Journal of Applied Fluid Mechanics, Vol. 18, No. 1, pp. 98-111, 2025.
Available online at www.jafmonline.net, ISSN 1735-3572, EISSN 1735-3645.
https://doi.org/10.47176/jafm.18.1.2757

Experimental Study of the Flow Characteristics on Corrugated Wall with Perforation

L. Yu, J. Sun†, K. Sun, P. Yuan and W. Chen

Department of Process Equipment and Control Engineering, Hebei University of Technology, Tianjin, 300401, China
National-Local Joint Engineering Laboratory for Energy Conservation in Chemical Process Integration and Resources Utilization, School of Chemical Engineering, Hebei University of Technology, Tianjin, 300130, China

†*Corresponding Author Email: cwy63@hebut.edu.cn*

ABSTRACT

In this study, the flow characteristics of two-dimensional corrugated walls with perforation are investigated using particle image velocimetry (PIV) experiments. Analysis of the flow on perforated corrugated walls at perforation ratios φ = 1%, 2.5%, 5%, 10% and the same wavelength Reynolds number, Re_λ, shows that the friction coefficient, C_f, decreases with increasing perforation ratio, φ, and the followability becomes more obvious, indicating that perforations on the corrugated wall can reduce the drag. Analysis of the dimensionless circulation, Γ_Q^+, reveals that the perforation effectively controls separation on the corrugated wall, which is consistent with observations of the recirculation area. After elucidating the mechanism of action of the perforation on the corrugated wall, the turbulence characteristics at different Reynolds numbers are explored for φ = 2.5% by varying the velocity of the flow field. When Re_λ = 8800, the free flow velocity is insufficient to achieve the inverse pressure gradient required to produce stable separation in the flow field. With an increase in Re_λ, the recirculation region in the time-averaged flow field becomes incomplete due to the effect of the perforation, and the turbulent fluctuation is also weakened. The following behavior of the friction coefficient, C_f, with the oscillations of the wave crest and trough also differs from the behavior observed with increasing wavelength Reynolds number, Re_λ.

Article History

Received April 6, 2024
Revised July 30, 2024
Accepted August 3, 2024
Available online November 6, 2024

Keywords:

Separation
Flow control
Turbulence flow
PIV
Wavy wall

1. INTRODUCTION

The flow behavior on complex surfaces has attracted the attention of many researchers owing to its unique flow morphology in mechanical design, topographic studies, and industrial applications. The corrugated wall is a typical model used to study the flow on complex surfaces, and studies exploring flows on corrugated walls are of great scientific and engineering value. For example, the spread of a wind turbine wake on hilly terrain can be simulated using a corrugated terrain with steep slopes (Yang et al., 2022). The corrugated configuration can also be used to simulate the inhibition of vortex shedding (Wang et al., 2023), drag reduction (Hu et al., 2024) and control of capillary rise (Ma et al., 2022). At the same time, the shape of the corrugation induces separation, changes the flow structures, and adjusts the scalar transport on the wall (Zhang et al., 2022). Channels in some micro-heat transfer equipment use corrugated wall pipes to accelerate boiling or enhance convective heat transfer (Wan et al., 2018; Sathish Kumar & Jayavel, 2020).

Numerous studies have explored the separation of solid corrugated walls. Buckles et al. (1984) used a Doppler laser velocimeter to measure the flow velocity, U, and pressure on a corrugated wall at the bottom of a channel, the ratio of the amplitude to wavelength corrugated wall was $2a/\lambda$ = 0.2, and the bulk Reynolds number Re_b = 12000. The results suggeated that turbulent separation occurred on large-amplitude corrugated walls. With regard to the separation phenomenon on two-dimensional corrugated walls, researchers observed separation in instantaneous flows. For example, Kuzan et al. (1989) and Cherukat et al. (1998) observed this phenomenon in their studies at $2a/\lambda$ = 0.05, 0.125, Re_b = 48,000, 85,000 and $2a/\lambda$ = 0.1, Re_b = 3460, respectively. They attributed the separation in the instantaneous flow field to the inverse pressure gradient on the corrugated wall. After Henn and Sykes (1999) defined the ratio of time occupied by a positive streamwise velocity, u, as the

NOMENCLATURE

a	amplitude of the corrugated plate	$\bar{v}$	dimensionless normal time-averaged velocity
C_f	friction coefficient	v'	normal fluctuation velocity
D	width of the perforation	W	width of the corrugated plate
h	half-height of the corrugated plate to side wall	x	streamwise direction
L	total length of the corrugated plate	y	normal direction
Q	Q criterion	y_w	normal height of the corrugated wall
Re_b	bulk Reynolds number	z	spanwise direction
Re_λ	wavelength Reynolds number	φ	perforation ratio
S	strain rate tensor	λ	wavelength of the corrugated plate
S_m	corrugated plate spanwise-normal projection area	ν	kinematic viscosity
S_t	area of the channel cross section	ρ_p	density of polyethylene microspheres
Tu	turbulence intensity	τ_x	dimensionless streamwise Reynolds stress
u	streamwise instantaneous velocity	τ_y	dimensionless normal Reynolds stress
$\bar{u}$	dimensionless streamwise time-averaged velocity	τ_{xy}	dimensionless Reynolds shear stress
u'	streamwise fluctuation velocity	ω	vorticity
u_*	friction velocity	Γ_Q^+	dimensionless vortex circulation
U_0	free flow velocity	Ω	vorticity tensor
v	normal instantaneous velocity	Ψ	corrugated plate blockage ratio

intermittency factor of turbulence related to the separation region, Jayaraman and Khan (2020) used direct numerical simulations to determine that negative velocity occurred when $2a/\lambda$ = 0.017, 0.022, and 0.033. Some researchers have related the position of the separation region to that of the shear layer above the trough (Buckles et al., 1984; Hamed et al., 2015). However, few studies have been conducted on the flow characteristics of corrugated walls after control is applied.

To explore the control of corrugated plates, studies commonly investigated the two-phase flow control of a thin-film flow with perforations on corrugated plates (Chen et al., 2017), use the method of heating corrugated plates to promote mixing on corrugated walls (Kuhn et al., 2010), or change the inclination angle of the corrugation to control the flow on corrugated walls (Li et al., 2016). To control the flow separation, perforation is a popular method that does not require any external energy input. For example, a slit in a blade can be designed to direct the airflow from the pressure side to the suction side (Ni et al., 2019; Wang et al., 2021). Similarly, Golubev et al. (2021) perforated a plate to alter the flow characteristics.

Therefore, this study focuses on the corrugated wall as a representative of complex walls, uses the perforation to control the flow on the corrugated walls, and analyzes the separation region and turbulent fluctuation on the corrugated wall.

2. EXPERIMENTAL SETUP

2.1 Experimental Channel

The experiments were performed in a low-velocity circulation channel composed of transparent acrylic plate. The length of the experimental section of the channel was 2600 mm, and the cross-section size was 500 mm × 600 mm, as shown in Fig. 1. A synchronization controller was used to connect the particle image velocimetry (PIV) operating system, laser, and camera to coordinate the operation of each component at the same frequency. The PIV operating system used in the laboratory was Davis8.4. The power part of the channel was composed of an axial flow pump and a paddle, and water velocity was controlled by changing the pump velocity. In the experiments, the height of the water surface in the channel was controlled at 500 mm, the water temperature was 20 °C, the viscosity coefficient of water was $\nu = 1 \times 10^{-6}$ m^2/s, and the corresponding turbulence intensity was approximately 0.8%.

2.2 Corrugated Plate Model

To better illustrate the position of the corrugated plate in the channel and the positions of the PIV system, camera and laser, a schematic diagram of the device is shown in Fig. 1(b). In this study, the coordinates (x, y, z) are used to represent the streamwise, normal, and spread directions of the corrugated plate, respectively; u (m/s) and v (m/s) are the streamwise and normal instantaneous velocities, respectively. The corrugated plate used in the experiment is made of 304 stainless steel with a thickness of 1 mm, length L = 1000 mm, and width W = 400 mm, as shown in Fig. 2 (a). The corrugated plates had sufficient width on both sides of the centerline to ensure two-dimensional experiments. The amplitude and wavelength were a = 4 mm and λ = 80 mm, respectively, the amplitude to wavelength ratio was $2a/\lambda$ = 0.1, and the whole corrugated plate had a total of 12 and 1/2 cycles. The surface of the corrugated plate was blackened such that it did not reflect the light emitted by the laser. The shape of the corrugated plate was determined using Eq. (1):

$$y_w = 4\cos(\pi x / 40) \tag{1}$$

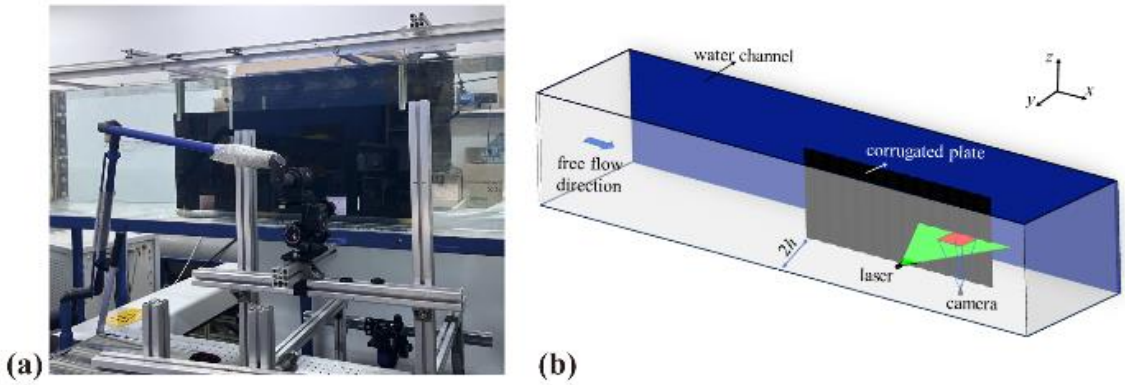

Fig. 1 Illustration of the experimental set-up

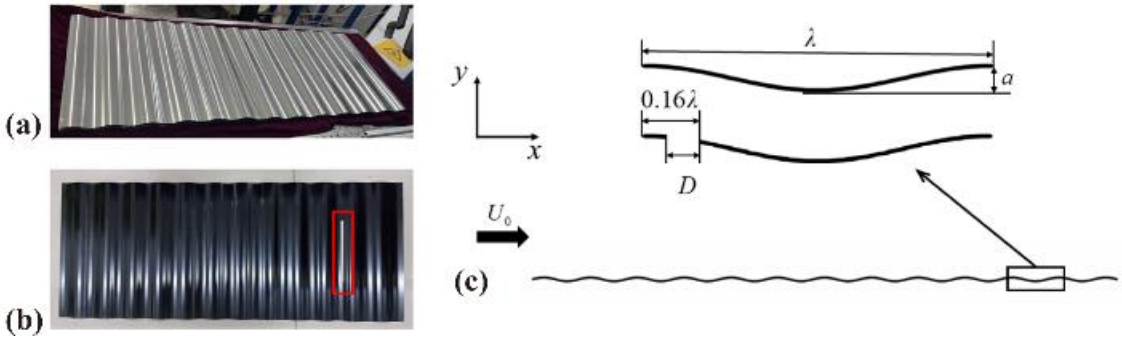

Fig. 2 Diagram of the corrugated plate

where y_w is the normal distance from the corrugated wall, and x is the streamwise distance along the corrugated wall. The bulk Reynolds number, Re_b, given by the bulk velocity, U_b, and the half-distance from the side wall of the channel to the corrugated wall, h, is given by Eq. (2). The wavelength Reynolds number, Re_λ, given by the free flow velocity, U_0, and the wavelength, λ, of the corrugated plate is shown in Eq. (3).

$$\mathrm{Re}_b = \frac{U_b \times h}{v} \tag{2}$$

$$\mathrm{Re}_\lambda = \frac{U_0 \times \lambda}{v} \tag{3}$$

The perforation ratio $\varphi = D/\lambda$ is the ratio of the perforation size to the wavelength, referring to the study of aerodynamic performance with varying airfoil perforation sizes performed by the researcher. The position of the perforation was based previous studied by Hao et al. (2023) and Belamadi et al. (2016), in which the perforation was located in front of the separation point. The corrugated plate was perforated by laser cutting; the performance of the material near the laser cutting seam was almost unaffected, and the workpiece deformation was small (Naresh & Khatak, 2022). The location of the separation point was determined after experiments with an unperforated corrugated plate. To ensure the two-dimensionality of the experiments, a rectangular perforation of 8 mm × 180 mm was cut using a laser before the separation point of x/λ = 0.16. The schematic diagram of the corrugated plate cut with a perforation ratio φ = 10% perforation ratio is shown in Fig. 2(c). The perforation dimensions of the corrugated plates with varying perforation ratios only differed in the streamwise dimension, with values of 0.01λ, 0.025λ, 0.05λ, and 0.1λ, while the spreadwise dimension remained constant at 180 mm.

2.3 Measurement Method

The laser system configuration used in the experiments was a dual-pulsed Nd: YAG, 532 nm green laser (LPY700) with an energy output of 100 mJ/pulse, which was used to produce a horizontally polarized point-source beam. The 1 mm light source emitted by the laser through the side wall of the channel was perpendicular to the horizontal plane of the corrugated plate, and the illuminated surface was parallel to the direction of fluid flow and coincided with the central symmetry line of the corrugated plate, as shown in Fig. 1(b). The recording medium was a CCD camera with a Nikon F-mount lens adapter and a resolution of 2048 × 2048 pixels. The camera was fixed to the bottom of the channel, and the camera lens plane was parallel to the plane illuminated by the laser. Additional details regarding this device are provided by Sun et al. (2019). To ensure the full development of the flow field, the shooting area was set at the eleventh cycle, and the shooting range included the entire cycle. The blockage rate of the corrugated plate in the streamwise direction of the channel was $\Psi = (S_m/S_t) \times 100\% = 1.28\%$, where S_m is the projection area of the corrugated plate in the spanwise -normal direction of the channel, and S_t is the cross-sectional area of the channel. The influence of the

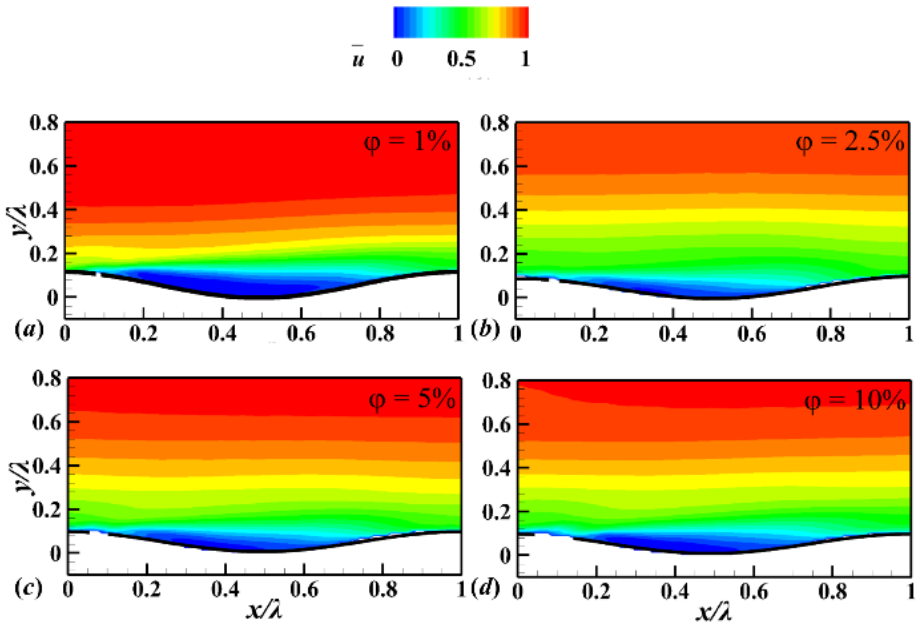

Fig. 3 Dimensionless streamwise time-averaged velocity fields: (*a*) φ = 1%; (*b*) φ = 2.5%; (*c*) φ = 5%; (*d*) φ = 10%

channel wall on the test results can be ignored (West & Apelt, 1982). Moreover, the distance between the upper and lower surfaces of the corrugated plate and the side wall of the channel was much larger than the amplitude of the corrugated plate, and thus the influence of the side wall of the channel on the experimental results was also considered to be negligible.

A single CCD camera was used for the recording. Polyethylene microspheres with a diameter of 15 μm, close to neutral buoyancy, and a density of ρ_p = 1.05 × 10^3 g/cm^3 were used as tracers in the experiments, as these have demonstrated good tracking performance in water. To ensure a sufficient area was captured on the surface of the corrugated plate, the total field of view (FOV) was 130 × 130 mm^2. A 10 mm distance at the bottom of the FOV was not illuminated by the laser, and this area was not included in the calculation; the total FOV encompassed the length and height of the entire corrugation cycle. The images were recorded using a two-frame double-exposure mode with a sampling frequency of 90Hz and an exposure time of 1542 μs. The total number of samples was 12,000, and the sampling time was greater than 100 s, which was sufficient to ensure convergence of the second-order velocity statistics. The size of the interrogation window used in the final calculation was 32 × 32 pixels, the overlap rate was 50%, and the spatial resolution was approximately 0.89 mm/vector. The uncertainty of the measured velocity was estimated to be < 1% (Raffel et al., 2018).

3. RESULTS AND DISCUSSION

3.1 Separation Characteristics at Different Perforation Ratios

Figure 3 shows the time-averaged velocity cloud diagram at perforation ratios of φ = 1%, 2.5%, 5% and 10% for a wavelength Reynolds number Re_λ = 14400 and bulk Reynolds number Re_b = 17000. The time-averaged velocity is made dimensionless using the free flow velocity, U_0. The flow field is clearly stratified, and the flow is fully developed, reaching a stable turbulent state. The separation region described by Kruse et al. (2006) can be observed. The separation and reattachment points can be judged according to the position where the streamwise time-averaged velocity is less than or equal to 0 ($\bar{u} \le 0$), those points at different perforation ratios are listed in Table. 1. The area of the separation region is the largest when the perforation ratio is φ = 1%. The time-averaged normal velocity cloud diagram is shown in Fig. 4. Similar to the streamwise velocity, the time-averaged normal velocity is also made dimensionless based on the free flow velocity, U_0. When the perforation ratio is φ = 1%, the normal flow of fluid with a high velocity ejected from the perforation significantly affects the flow of the upper layer of the corrugated wall, causing the velocity of the normal flow to increase. This also explains why the largest separation region occurs at a perforation ratio of φ = 1%. This may be because the perforation ratio is small, and thus the fluid at the bottom of corrugated wall undergoes a dramatic transformation in the windward side. When the perforation ratio is φ = 2.5%, the effect of the perforation on the normal velocity is minimal, the normal velocity cloud diagram is most similar to the unperforated corrugated wall (Hamed et al., 2015). With the increase of the perforation ratio, the effect of the

Table 1 Separation and reattachment points at different perforation ratios

φ	separation point x/λ	reattachment point x/λ
1%	0.2	0.68
2.5%	0.25	0.42
5%	0.28	0.56
10%	0.16	0.6

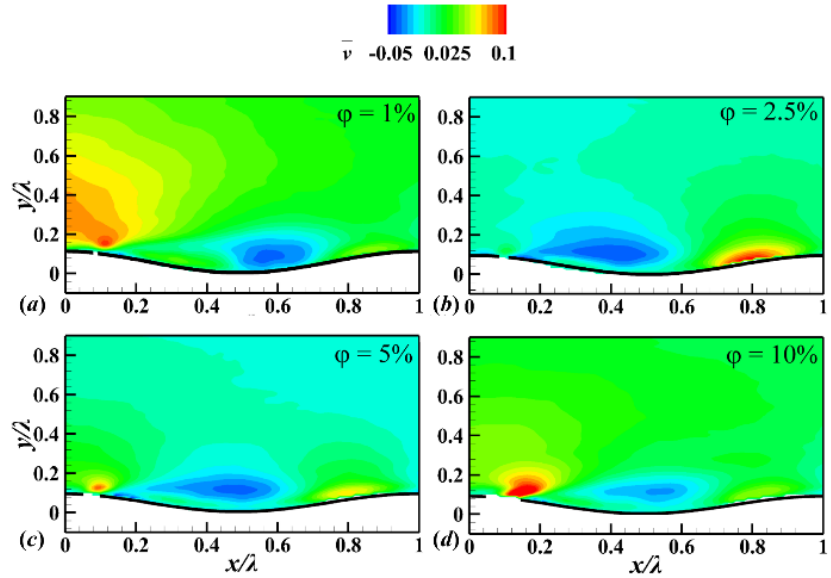

Fig. 4 Dimensionless normal time-averaged velocity fields: (*a*) φ = 1%; (*b*) φ = 2.5%; (*c*) φ = 5%; (*d*) φ = 10%

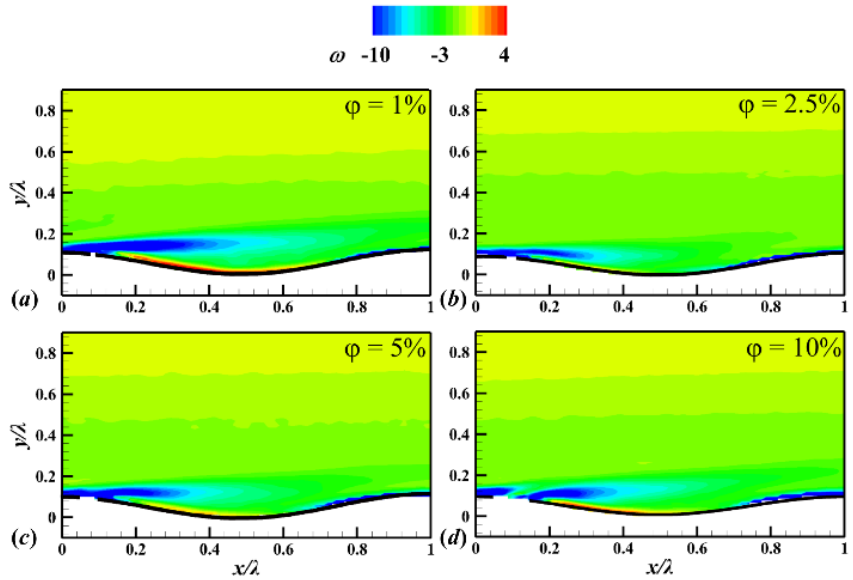

Fig. 5 Time-averaged vorticity on corrugated walls: (*a*) φ = 1%; (*b*) φ = 2.5%; (*c*) φ = 5%; (*d*) φ = 10%

perforation on the normal velocity increases. When the perforation ratio is φ = 10%, the normal velocity of the perforation position is the maximum, and the free flow velocity affects the jet fluid. The area of the separation region also increases. When the wavelength Reynolds number is Re_λ = 14400, a perforation ratio of φ = 2.5% is selected to control the separation effect on the corrugated wall.

Owing to the unique wave characteristics of corrugated walls, the separation depends on the shape of the wall boundary. To verify the strength of the separation, the vorticity is calculated for different perforation ratios of φ = 1%, 2.5%, 5%, and 10% is calculated, and the change in the non-dimensional vorticity circulation, Γ_Q^+, is determined. The mean flow dimensionless vorticity circulation is determined using Eq. (4),

$$\Gamma_Q^+ = \int_L \left|\overline{\omega}\right| \frac{\lambda}{U_0} dL \tag{4}$$

where L represents the curve closed by the vorticity down to the maximum value of 5%, which is calculated using the Q criterion (Joseph et al., 2020). This represents the maximum value of the second invariant of the velocity gradient tensor, as shown in Eq. (5) proposed by Hunt et al. (1988), to identify the vortex structures in the flow field.

$$Q = \frac{1}{2}\left(\|\Omega\|^2 - \|S\|^2\right) \tag{5}$$

where Ω = ($\partial u/\partial y$ - $\partial u/\partial y$)/2 represents the vorticity tensor, and S = ($\partial u/\partial y$ + $\partial u/\partial y$)/2 represents the strain rate tensor.

Figure. 5 shows the time-averaged vorticity cloud diagram, positive vorticities indicate counterclockwise rotation and negative vorticities indicate clockwise rotation. The vortex starts to develop after the crest, and the high clockwise vorticity region is highly consistent with the time-averaged velocity. This also shows that the

Table 2 Dimensionless vortex circulation on corrugated walls with different perforation ratios

φ	$\Gamma_Q^+(\times 10^{-3})$
1%	1.04
2.5%	0.34
5%	0.54
10%	0.88

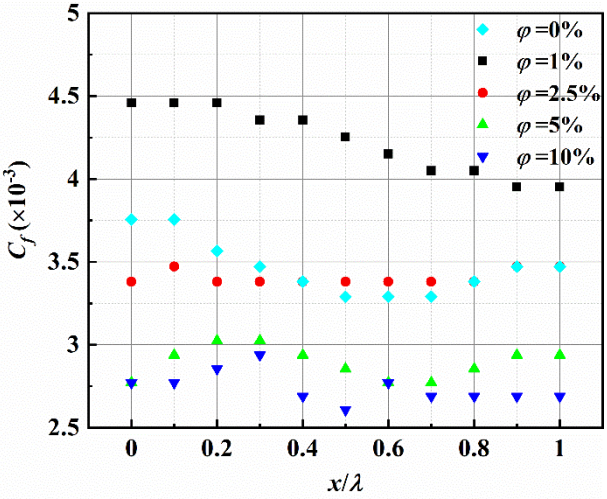

Fig. 6 Friction coefficients, C_f, of corrugated walls with different perforation ratios

disturbance of the flow field is more intense when the perforation ratio is φ = 1%, and thus the separation phenomenon is more obvious.

The dimensionless vortex circulation at perforation ratios of φ = 1%, 2.5%, 5%, and 10% are shown in Table 2. The vortex circulation is the largest when the perforation ratio is φ = 1%. When the perforation ratio is φ = 2.5%, the results are consistent with those obtained in the time-averaged velocity field, and the smallest vortex circulation is observed. As the perforation ratio increases, the vortex circulation gradually increases, similar to the area of the separation region obtained previously.

3.2 Statistical Characteristics of Turbulence at Different Perforation Ratio

Figure 6 shows the friction coefficient, C_f, at perforation ratios of φ = 1%, 2.5%, 5%, and 10%, the calculation equation is as shown in eq. (6),

$$C_f = 2\left(\frac{u_*}{U_0}\right)^2 \tag{6}$$

where u_* is the friction velocity of corrugated walls. The friction velocity can be obtained by a graphical method based on nonlinear least squares error fitting (Clauser, 1954).

Eleven equidistant points are selected along the streamwise direction at 0.1λ intervals to calculate the friction coefficient of the entire corrugated wall. As shown in Fig. 6, when the perforation ratio φ = 1%, the friction coefficient exhibits a wavy linear variation pattern, similar to that of the corrugated wall. When the perforation ratio is increased to φ = 2.5%, this wavy linear change disappears and becomes smoother, which also effectively illustrates that a perforation ratio φ = 2.5% reduces the velocity fluctuation in the corrugated cycle. This wavy linear change exhibits a clear fluctuation, which is more strongly attached to the corrugated wall. At the same time, Fig. 6 shows that the friction coefficient on the corrugated walls exhibits a decreasing trend with an increase in the perforation ratio, indicating that the friction drag on the corrugated walls decreases with increasing perforation ratio. Compared with φ = 0%, the other conditions (except φ = 1%) have the effect of reducing the friction drag.

To observe the turbulent fluctuation levels at perforation ratios of φ = 1%, 2.5%, 5%, and 10%, the turbulence intensities, *Tu*, at different perforation ratios are shown in Fig. 7. As shown in Fig. 7, the maximum value of the turbulence intensity occurs directly above the trough, extending from the leeward side to the crest of the next cycle, and the influence range spans the entire corrugation cycle. As shown in Fig. 7(a), when the perforation ratio is φ = 1%, the turbulent fluctuation

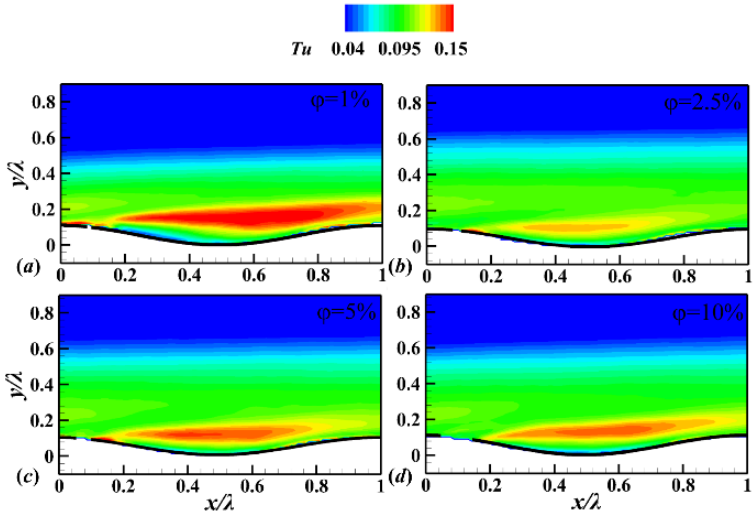

Fig. 7 Cloud diagram of the turbulence intensity distribution on corrugated walls: (*a*) φ = 1%; (*b*) φ = 2.5%; (*c*) φ = 5%; (*d*) φ = 10%

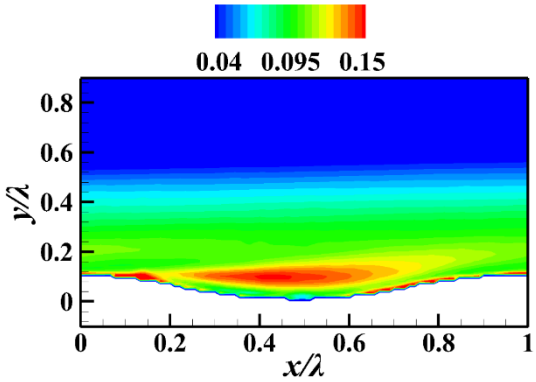

Fig. 8 Cloud diagram of the turbulence intensity distribution on the corrugated wall without perforation

extends to the next corrugation cycle. When the perforation ratio increases to φ = 2.5%, the turbulence intensity is significantly weakened, and the flow fluctuation is minimal; however, the main concentration region remains above the trough.

The turbulence intensity distribution on the corrugated wall without perforation is shown in the Fig. 8. A comparsion with the turbulence intensity on the perforated corrugated wall in Fig. 7, shows that except for the case of φ = 1%, the other three perforation ratios effectively reduce the turbulence fluctuation on the corrugated wall. This result indicates that a perforation ratio of φ = 1% can enhance the momentum exchange on the corrugated wall, while perforation ratios of φ = 2.5%, 5%, and 10% can effectively weaken the turbulence fluctuation on the corrugated wall and achieve the effect of reducing turbulence.

The Reynolds stresses at perforation ratios of φ = 1%, 2.5%, 5%, and 10% are shown in Fig. 9. Fig. 9(a_1-d_1) show the streamwise Reynolds stress, Fig. 9(a_2-d_2) show the normal Reynolds stress, and Fig. 9(a_3-d_3) show the Reynolds shear stress.

Figure. 9(a_1-d_1) show that when the perforation ratio is φ = 1%, a weakly fluctuating fluid enters the flow field from the perforation and flows through the trough. This occurs because the perforation improves the momentum exchange between the high and low-velocity fluids in the

trough, which causes the shear layer above the wall to change. Therefore, the shear layer with a high Reynolds number becomes thicker when the perforation ratio is φ = 1%. Moreover, the area of influence increases. When the perforation ratio is increased to φ = 2.5%, the perforation ratio is just sufficient to impact the momentum of the high-velocity fluid below the

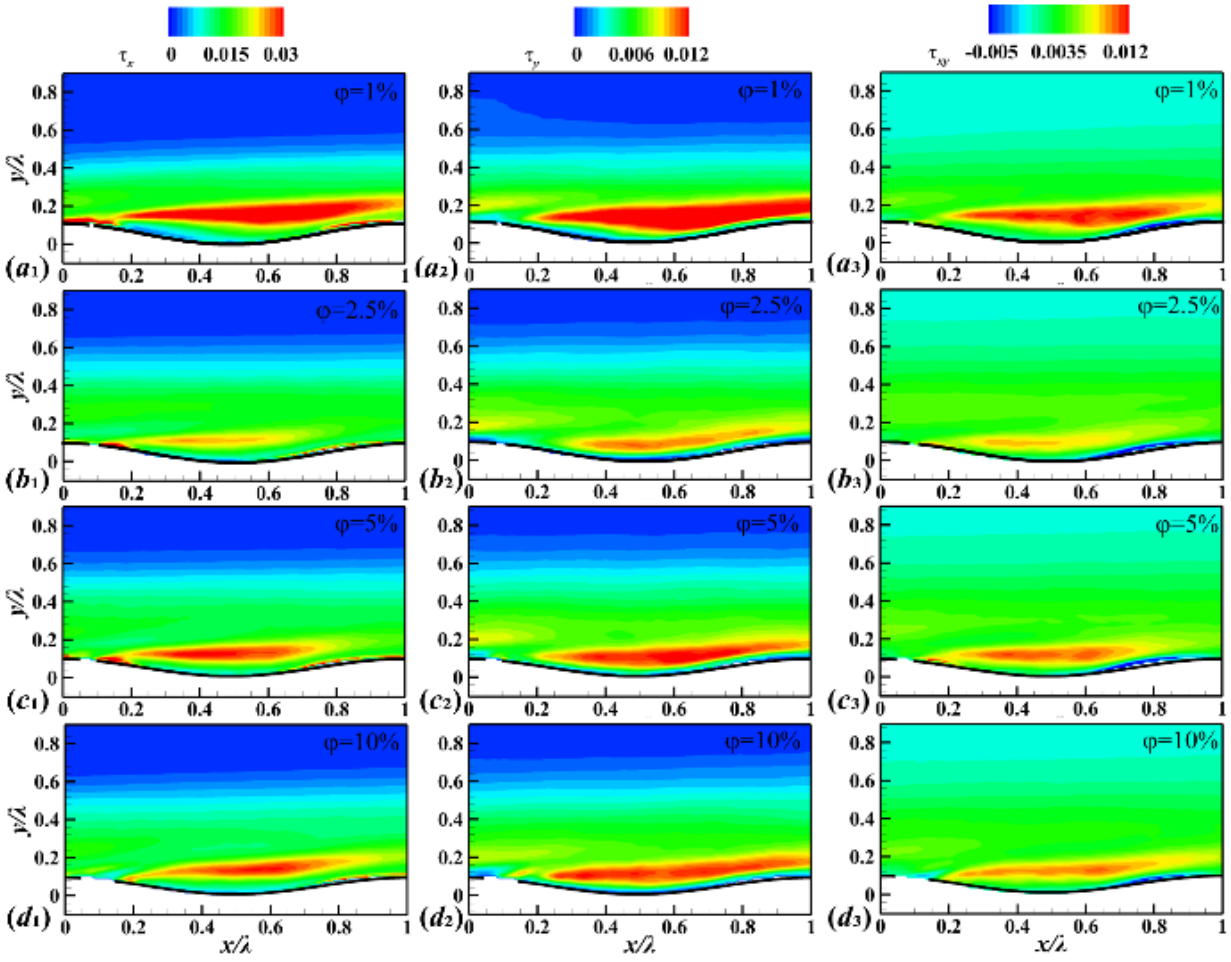

Fig. 9 Cloud diagram of the Reynolds stress distributions on corrugated walls: (a_1) - (a_3) φ = 1%; (b_1) - (b_3) φ = 2.5%; (c_1) - (c_3) φ = 5%; (d_1) - (d_3) φ = 10%

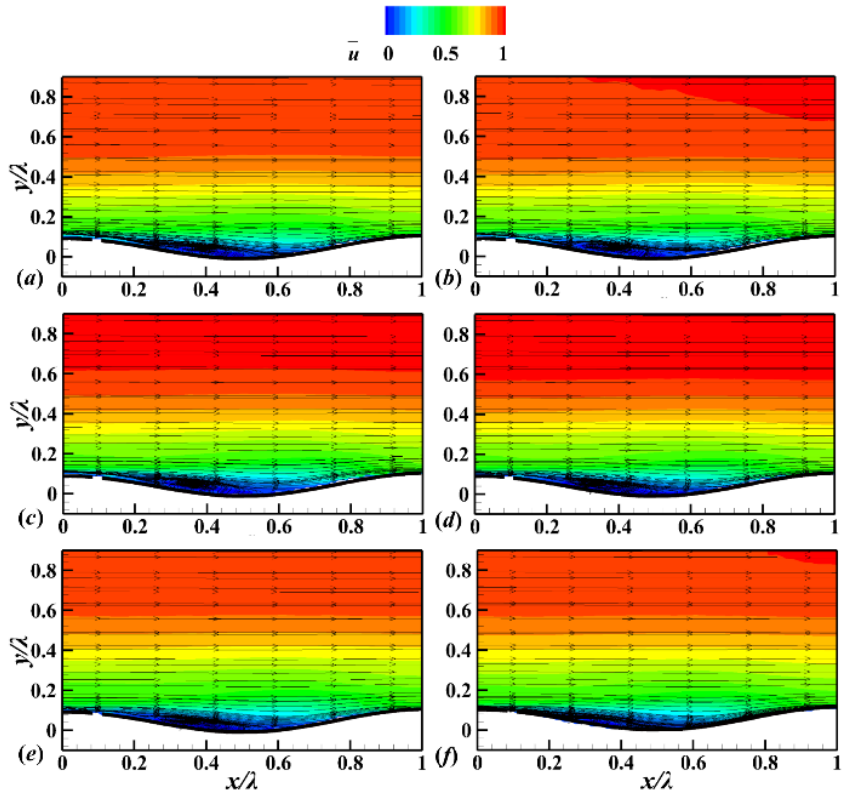

Fig. 10 Dimensionless streamwise time-averaged velocity fields: (*a*) Re_λ = 5600; (*b*) Re_λ = 7200; (*c*) Re_λ = 8800; (*d*) Re_λ = 10400; (*e*) Re_λ = 12800; (*f*) Re_λ = 14400

corrugated wall into the flow field above the corrugated wall, the shear layer is thinned, and the fluid fluctuation in the near-wall region is reduced. With an increase in the perforation ratio, more high-velocity fluid enters the flow field above the corrugated wall, which intensifies the momentum exchange and streamwise fluctuation in the flow field. As shown in Fig. 9 (a_2-d_2), the normal fluctuation in the flow field exhibitis the same trend as the streamwise fluctuation. When the perforation ratio is φ =1%, the momentum exchange at the trough is the most severe because the high-velocity fluid flows along the wall at the trough. However, the normal fluctuation is primarily concentrated in the trough, and the range of the fluctuation extends to the trough of the next corrugation cycle.

For the Reynolds shear stresses shown in Fig. 9(a_3-d_3), the high Reynolds stress region is associated with the shear layer in the x/λ = 0.2 – 0.95 and y/λ = 0.1 – 0.2 regions at φ = 1%, whereas the Reynolds shear stress is lowest at φ = 2.5%. Only a small region of high Reynolds stress is present at x/λ = 0.3 – 0.55 and y/λ = 0.08 – 0.12. When φ = 5%, this region is located at x/λ = 0.2 – 0.75 and y/λ = 0.08 – 0.2. When φ = 10%, it is located at x/λ = 0.2 – 0.8 and y/λ = 0.1 – 0.2. The negative Reynolds shear stress region in upstream and downstream of the wave, which is a Cartesian coordinate system product reported by Hudson et al. (1996) and Cherukat et al. (1998), also appears at these perforation ratios. In their view, such a phenomenon does not occur in the boundary layer coordinate system.

3.3 Separation Characteristics at Different Reynolds Numbers

The streamwise and normal time-averaged velocity cloud diagrams at different Reynolds numbers are shown in Figs. 10 and 11, respectively, for a perforation ratio of φ = 2.5%. In Figs. 10 and 11, (*a*) – (*f*) are the wavelength Reynolds numbers Re_λ = 5600 – 14400 and corresponding bulk Reynolds numbers Re_b = 6647 – 17500, respectively. The time-averaged velocity is made dimensionless using the free flow velocity U_0. The separation and reattachment points at different Reynolds numbers are listed in Table. 3. As the Reynolds number increases, the separation point does not change significantly; however, the reattachment point is delayed. In contrast to the other perforation ratios, at the perforation ratio of φ = 2.5%, the separation region is less complete at the six Reynolds numbers, as shown by the streamlines in Fig. 10, presumably because the flow velocity is too low. Similarly, as mentioned in the introduction, Zilker and Hanratty (1979) stated that when $2a/\lambda > 0.03$, whether separation occurs is strongly related to the Reynolds number, as shown in the time-averaged normal velocity cloud diagram in Fig. 11. When the wavelength Reynolds number is Re_λ = 5600, the fluid ejected from the perforation has the largest range of impact, and thus the separation area is the largest. However, there is no maximum span in the separation region because the wavelength Reynolds number is small. As the wavelength Reynolds number increases to Re_λ = 8800, the normal time-averaged velocity decreases, leading to a decrease in the area of the separation region.

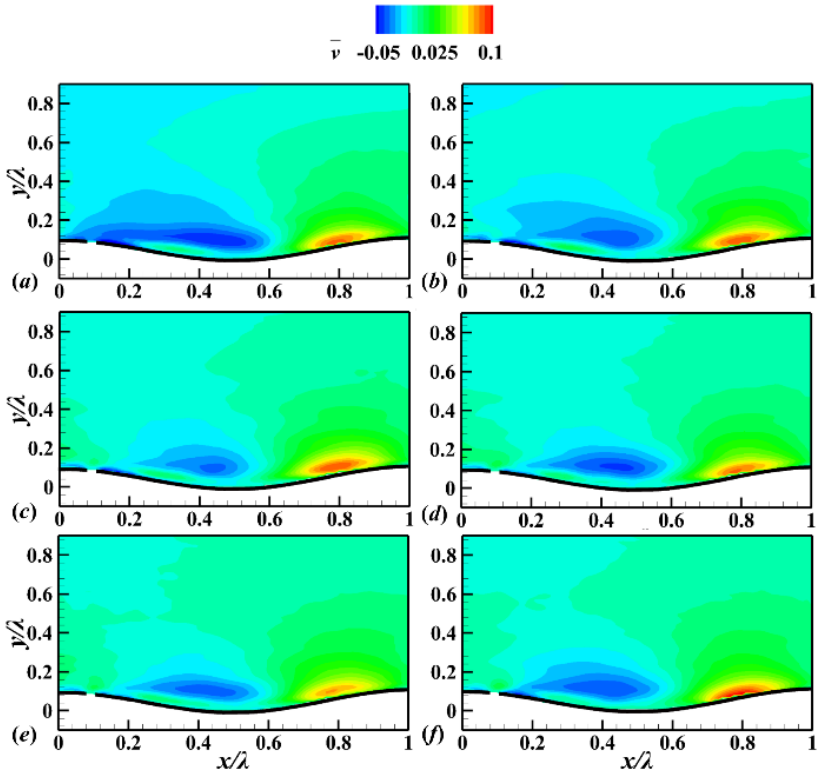

Fig. 11 Dimensionless normal time-averaged velocity fields: (a) Re_λ = 5600; (b) Re_λ = 7200; (c) Re_λ = 8800; (d) Re_λ = 10400; (e) Re_λ = 12800; (f) Re_λ = 14400

Table 3 Separation and reattachment points at different Reynolds numbers

Re_λ	Re_b	separation point x/λ	reattachment point x/λ
5600	6647	0.25	0.52
7200	8730	0.25	0.52
8800	10734	0.25	0.56
10400	12855	0.25	0.56
12800	14748	0.25	0.6
14400	17500	0.25	0.42

Table 4 Dimensionless vortex circulation on corrugated walls with different wavelength Reynolds numbers

Re_λ	Re_b	Γ_Q^+(× 10^{-4})
5600	6647	3.52
7200	8730	3.72
8800	10734	3.36
10400	12855	3.83
12800	14748	4.20
14400	17500	3.40

Moreover, it can be observed from the streamlines that the separation region does not form a complete recirculation region when it is extremely close to the corrugated wall. When the wavelength Reynolds number increases to Re_λ = 14400, the span and area of the separation region are weakened, and the recirculation region is no longer formed, which reduces the separation on the corrugated wall.

Because no complete recirculation region is formed when the perforation ratio is φ = 2.5%, to further verify the separation region described, the dimensionless vortex circulation, Γ_Q^+ , is used to illustrate the separation strength at different wavelength Reynolds numbers Re_λ = 5600 – 14400. As indicated in Table 4, the dimensionless vortex circulation is smallest when Re_λ = 8800, and the separation strength and area are also the smallest under this condition. Moreover, the maximum dimensionless vortex circulation appears at Re_λ = 12800, and the separation area is the largest, which also indicates that the recirculation ability is the strongest to drive the momentum transfer on the corrugated wall.

3.4 Statistical Characteristics of Turbulence at Different Reynolds Numbers

The friction coefficient, C_f, at different wavelength Reynolds numbers Re_λ = 5600 – 14400 are shown in Fig. 12. Along the streamwise direction, friction coefficient C_f is calculated and compared for the entire perforated corrugated wall by selecting 11 equidistant points at intervals of 0.1λ.

As shown in Fig. 12, when the wavelength Reynolds number Re_λ = 7200, 8800, and 10400, the friction coefficients more closely follow the corrugated wall than with the other three wavelength Reynolds numbers. When the leeward and windward sides are close to the wave peak, the friction coefficient on the side is greater than that at the trough. When the wavelength Reynolds number Re_λ = 5600, 12800, and 14400, the friction coefficient changes gradyally over the whole corrugation

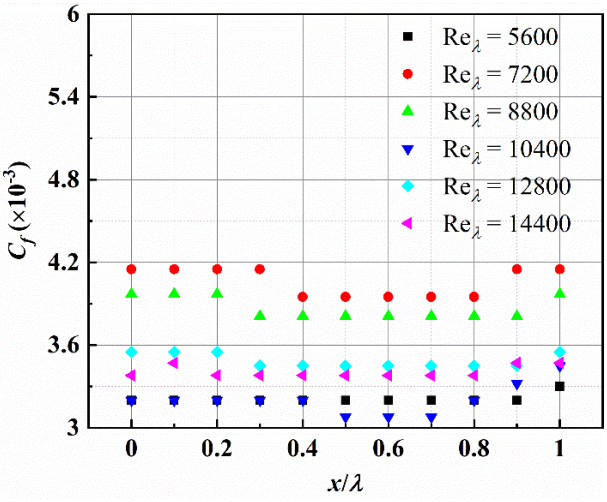

Fig. 12 Friction coefficients, C_f, of corrugated walls with different wavelength Reynolds numbers

cycle, and it changes only slightly on the leeward and windward sides near the wave peak, thus indicating that the uneven distribution of friction drag on the perforated corrugated wall can be improved. The friction coefficient is relatively low at these three wavelength Reynolds numbers. This can provide a more convenient drag reduction scheme in engineering practice.

To observe the turbulent fluctuation level at six wavelength Reynolds numbers of Re_λ = 5600 – 14400, the turbulence intensity, *Tu*, are shown in Fig. 13. Consistent with the previous case, the concentration area of the turbulent fluctuation is still directly above the trough; however, with a change in the wavelength Reynolds number, the range of the turbulent fluctuation on the perforated corrugated walls becomes strong or weak. When the wavelength Reynolds number is Re_λ = 5600 – 12800, the turbulence intensity cloud diagram clearly shows the presence of a small region of fluction on the leeward side of the trough close to the wall, which is due to the slight fluctuation of the original recirculation region caused by the high-velocity fluid ejected into the low-velocity fluid above the corrugated wall after the perforation. However, the shear layer described by Buckles et al. (1984) is generated. Thus, the recirculation region still exists, but it is no longer a recirculation region close to the wall, which corresponds to the incomplete separation region described previously. When the wavelength Reynolds number increases to Re_λ = 14400, the high-velocity fluid ejecting into the upper part of the corrugated wall no longer affects the fluid near the wall; however, the recirculation region is no longer complete because of the weak shear layer. This also explains why no complete separation region is formed at the perforation ratio of φ = 2.5% and wavelength Reynolds number Re_λ = 14400.

Under a perforation ratio φ = 2.5%, the Reynolds stresses at six wavelength Reynolds numbers Re_λ = 5600 – 14400 are shown in Fig. 14. Fig. 14(a_1-f_1) show the streamwise Reynolds stress, Fig. 14(a_2-f_2) show normal Reynolds stress, and Fig. 14(a_3-f_3) show Reynolds shear stress. The streamwise Reynolds stress cloud diagrams in

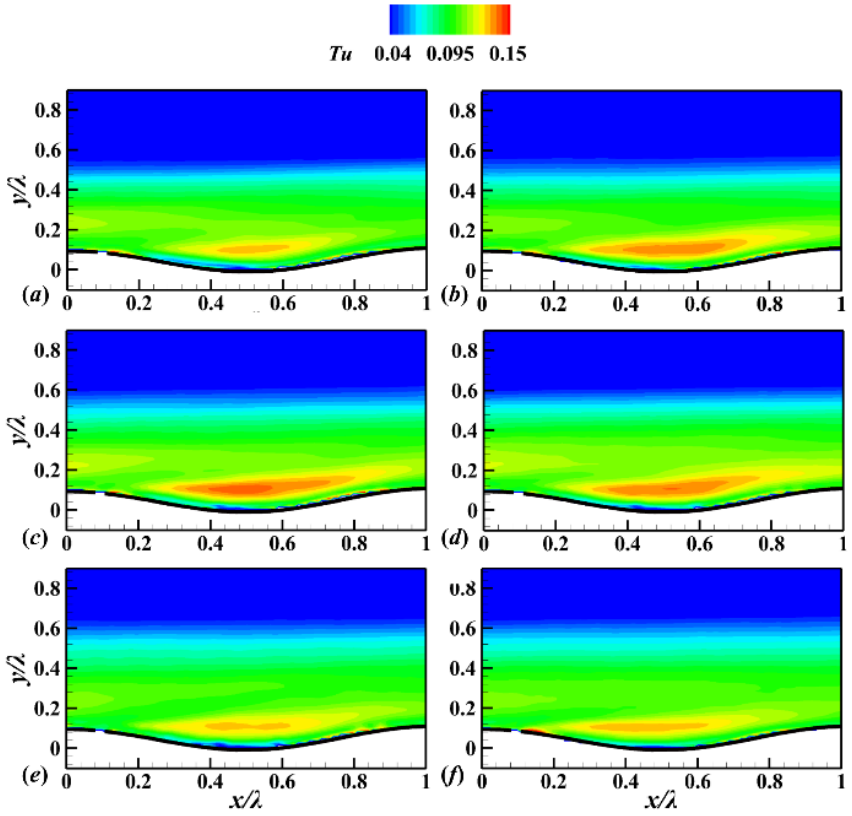

Fig. 13 Cloud diagram of the turbulence intensity distribution on corrugated walls: (*a*) Re_λ = 5600; (*b*) Re_λ = 7200; (*c*) Re_λ = 8800; (*d*) Re_λ = 10400; (*e*) Re_λ = 12800; (*f*) Re_λ = 14400

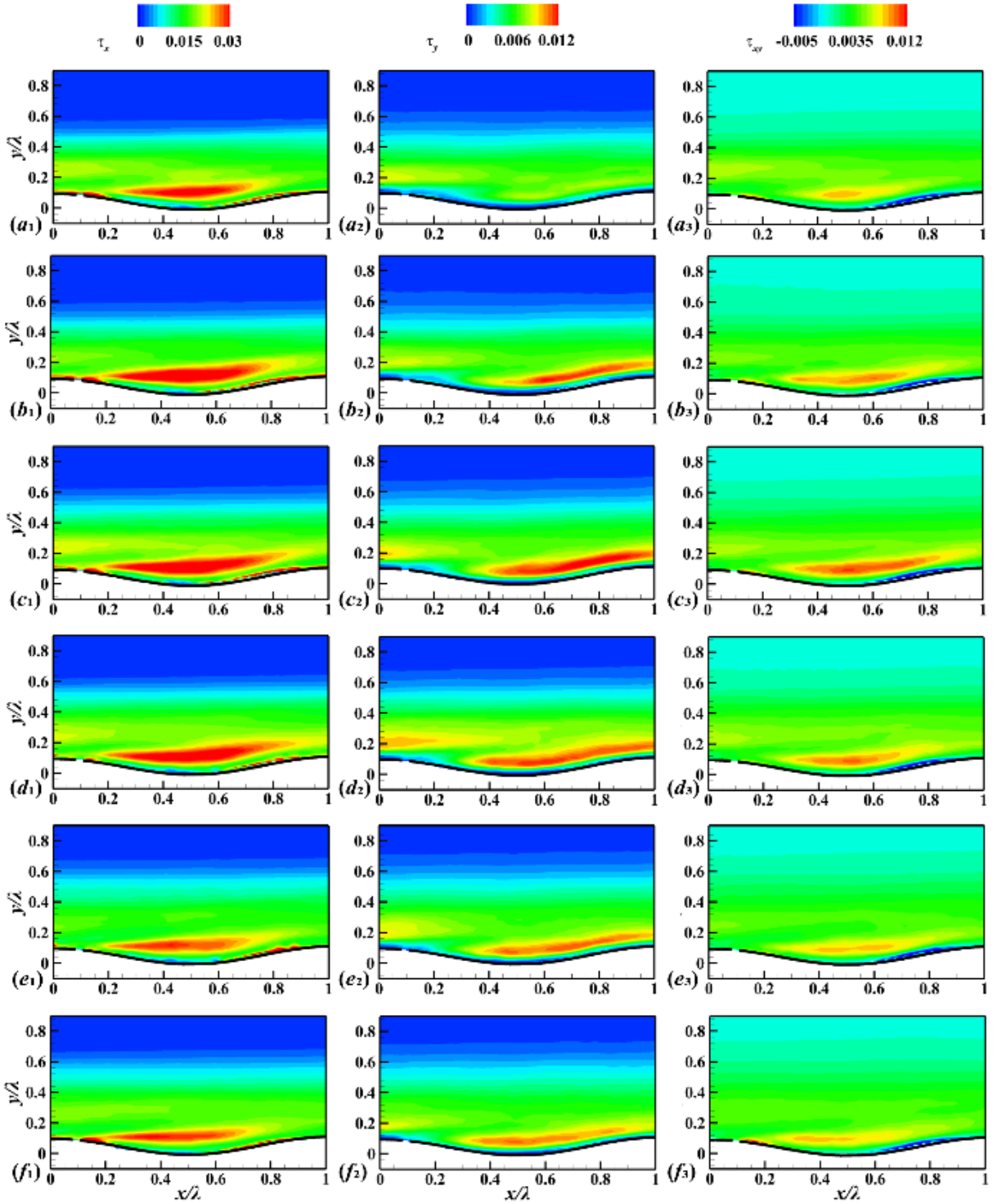

Fig. 14 Cloud diagram of the Reynolds stress distribution on corrugated walls: (*a*) Re_λ = 5600; (*b*) Re_λ = 7200; (*c*) Re_λ = 8800; (*d*) Re_λ = 10400; (*e*) Re_λ = 12800; (*f*) Re_λ = 14400

Figure 14(a_1-f_1) show that when the wavelength Reynolds number is Re_λ = 5600 – 10400, a large streamwise Reynolds stress is generated, which indicates that the streamwise fluctuation velocity is relatively large. Consequently, the span of the separation region at these four working cases is not significantly weaker than that in the latter two working cases. When the wavelength Reynolds number increases, there is a sufficient inverse pressure gradient for separation, but the perforation reduces the streamwise fluctuation of the fluid; therefore, the streamwise Reynolds stress (the inertial force of the streamwise flow), does not change significant change. The normal Reynolds stress in Fig. 14(a_2-f_2) clearly shows that when the wavelength Reynolds number is Re_λ = 5600, the near-wall region of the corrugated wall exhibits a slight fluctuation. A trend of normal fluctuation enhancement is observed at the perforation. However, because the free flow velocity is low, the perforation does not lead to a special normal fluctuation. With increasing Re_λ, the effect of the

perforation on the normal fluctuation becomes more intense. When the wavelength Reynolds number increases to Re_λ = 14400, the perforation completely affects the normal fluctuation in the near-wall region of the corrugated wall, and the normal Reynolds stress is weakened.

The leeward side is mainly a low-momentum region, while the high-momentum region is located above the trough. The junction of the high and low-momentum regions occurs at the position where the streamwise velocity gradient is 0; therefore, this is also the position where the separation occurs. After perforation, the high-momentum fluid on the corrugated wall is ejected into the low-momentum region. When the wavelength Reynolds number is Re_λ = 5600, the high-momentum fluid is not sufficient to have an impact on the shear layer. Therefore, as the wavelength Reynolds number, Re_λ, increases, the momentum of the fluid ejected into the upper part of the corrugated wall also increases, which is sufficient to affect the shear layer of the flow field. However, when the wavelength Reynolds number gradually increases to Re_λ = 10400, the low-momentum fluid on the leeward side is removed by the high-momentum fluid. This is also the principle obtained by perforation to increase the velocity gradient used in the control of airfoil separation.

4. CONCLUSION

In this study, the separation characteristics and turbulence statistics of two-dimensional corrugated walls were analyzed for different perforation ratios and Reynolds numbers using PIV experiments. The conclusions are as follows:

(1) At the same wavelength Reynolds number Re_λ = 14400 and the same bulk Reynolds number Re_b = 17500, the recirculation area caused by the separation on the leeward side of the corrugated wall will be affected by changing the perforation ratio of the corrugated wall. The turbulence characteristics shows that a perforation ratio of φ = 1% leads to an increase in the circulation and improves the momentum transport between the peaks of the corrugated walls. When the perforation ratio is increased to φ = 2.5%, the shear layer above the trough is thinned, and the separation region on the corrugated wall is no longer obvious, thus inhibiting the fluctuation and separation on the corrugated wall. Moreover, a perforation ratio of φ = 10% plays an important role in reducing the drag of the corrugated wall.

(2) At a perforation ratio of φ = 2.5%, when the wavelength Reynolds number is Re_λ = 5600, the free flow velocity is too low to achieve a sufficient adverse pressure gradient to cause a stable separation phenomenon. However, the turbulent fluctuation intensity is relatively high. When the wavelength Reynolds number increases to Re_λ = 10400 or greater, separation begins to occur above the perforated corrugated wall due to the existence of an inverse pressure gradient, but the separation remains incomplete owing to the combined effect of perforation and the increasing wavelength Reynolds number.

As a representative of complex walls, perforation on corrugated walls have different influences on flow separation control at different perforation ratios, as for the flow control of slits in the blade. According to the results of this study, perforation on a corrugated wall can effectively control the uneven distribution of friction drag, which provides guidance for the reduction of drag on complex walls. The results at different perforation ratios provide a reference for improving the heat transfer efficiency of corrugated wall heat exchangers and reducing flow separation or drag in corrugated pipes.

ACKNOWLEDGEMENTS

This research was supported by the National Natural Science Foundation of China [Grant numbers 11602077, and 11572357] and the Natural Science Foundation of Hebei Province [Grant number A2021202009].

CONFLICT OF INTEREST

The authors declare that they have no known competing financial interests or personal relationships that could have appeared to influence the work reported in this paper.

AUTHORS CONTRIBUTION

Linmeng Yu: Writing – original draft, Investigation, Conceptualization, Methodology, Formal analysis, Data curation. **Jiao Sun:** Conceptualization, Methodology, Resources, Writing – review & editing, Funding acquisition, Supervision. **Kangfu Sun:** Writing – review & editing, Methodology, Investigation. **Pengda Yuan:** Investigation, Data curation. **Wenyi Chen:** Investigation, Conceptualization, Methodology, Resources, Funding acquisition, Supervision.

REFERENCES

Belamadi, R., Djemili, A., Ilinca, A., & Mdouki, R. (2016). Aerodynamic performance analysis of slotted airfoils for application to wind turbine blades. *Journal of Wind Engineering and Industrial Aerodynamics*, *151*, 79–99. https://doi.org/10.1016/j.jweia.2016.01.011

Buckles, J., Hanratty, T. J., & Adrian, R. J. (1984). Turbulent flow over large-amplitude wavy surfaces. *Journal of Fluid Mechanics*, *140*, 27–44. https://doi.org/10.1017/S0022112084000495

Chen, S., Ma, J., Zhang, X., & Chen, W. (2017). Numerical simulation of the behavior of high-viscosity fluids falling film flow down the vertical wavy wall. *Asia-Pacific Journal of Chemical Engineering*, *12*, 97–109. https://doi.org/10.1002/apj.2057

Cherukat, P., Na, Y., Hanratty, T. J., & McLaughlin, J. B. (1998). Direct numerical simulation of a fully developed turbulent flow over a wavy wall. *Theoretical and Computational Fluid Dynamics*, *11*(2), 109–134.

https://doi.org/10.1007/s001620050083

Clauser, F. H. (1954). Turbulent boundary layers in adverse pressure gradients. *Journal of the Aeronautical Sciences*, *21*(2), 91–108. https://doi.org/10.2514/8.2938

Golubev, A. G., Golubev, G., Stolyarova, E. G., & Kalugina, M. D. (2021). Research of the airflow process around a perforated plate when changing the value of its thickness. *AIP Conference Proceedings*, *2318*(1), 110010. https://doi.org/10.1063/5.0037185

Hamed, A. M., Kamdar, A., Castillo, L., & Chamorro, L. P. (2015). Turbulent boundary layer over 2D and 3D large-scale wavy walls. *Physics of Fluids*, *27*(10), 106601. https://doi.org/10.1063/1.4933098

Hao, L., Lin Z., Qu, H., Wang, J., & Gao, Y. (2023). Influence of slot geometry configuration on airfoil aerodynamic characteristics. *Acta Aerodynamica Sinica*, *41*(11), 1–10. https://dx.doi.org/10.7638/kqdlxxb-2022.0188

Henn, D. S., & Sykes, R. I. (1999). Large-eddy simulation of flow over wavy surfaces. Journal of Fluid Mechanics, 383, 75–112. https://doi.org/10.1017/S0022112098003723

Hu, C., Gu, Y., Zhang, J., Qiu, Q., Ding, H., Wu, D., & Mou, J. (2024). Research on the flow and drag reduction characteristics of surfaces with biomimetic fitting structure. *Journal of Applied Fluid Mechanics*, *17*(8), 1593–1603. https://doi.org/10.47176/jafm.17.8.2591

Hudson, J. D., Dykhno, L., & Hanratty, T. J. (1996). Turbulence production in flow over a wavy wall. *Experiments in Fluids*, *20*(4), 257–265. https://doi.org/10.1007/BF00192670

Hunt, J., Wray, A., & Moin, P. (1988). *Eddies, streams, and convergence zones in turbulent flows*. Studying Turbulence Using Numerical Simulation Databases.

Jayaraman, B., & Khan, S. (2020). Direct numerical simulation of turbulence over two-dimensional waves. *AIP Advances*, *10*(2), 025034. https://doi.org/10.1063/1.5140000

Joseph, L. A., Molinaro, N. J., Devenport, W. J., & Meyers, T. W. (2020). Characteristics of the pressure fluctuations generated in turbulent boundary layers over rough surfaces. *Journal of Fluid Mechanics*, *883*, A3. https://doi.org/10.1017/jfm.2019.813

Kruse, N., Kuhn, S., & Von Rohr, P. R. (2006). Wavy wall effects on turbulence production and large-scale modes. *Journal of Turbulence*, *7*, N31. https://doi.org/10.1080/14685240600602911

Kuhn, S., Kenjereš, S., & Rudolf von Rohr, P. (2010). Large eddy simulations of wall heat transfer and coherent structures in mixed convection over a wavy wall. *International Journal of Thermal Sciences*, *49*(7), 1209–1226. https://doi.org/10.1016/j.ijthermalsci.2010.01.017

Kuzan, J. D., Hanratty, T. J., & Adrian, R. J. (1989). Turbulent flows with incipient separation over solid waves. *Experiments in Fluids*, *7*(2), 88–98. https://doi.org/10.1007/BF00207300

Li, Q., Wang, T., Dai, C., & Lei, Z. (2016). Hydrodynamics of novel structured packings: An experimental and multi-scale CFD study. *Chemical Engineering Science*, *143*, 23–35. https://doi.org/10.1016/j.ces.2015.12.014

Ma, B., Li, D., & Yang, H. (2022). Analytical and numerical study of capillary rise in sinusoidal wavy channel: Unveiling the role of interfacial wobbling. *Physics of Fluids*, *34*(5), 052114. https://doi.org/10.1063/5.0092613

Naresh & Khatak, P. (2022). Laser cutting technique: A literature review. *Materials Today: Proceedings*, *56*, 2484–2489. https://doi.org/10.1016/j.matpr.2021.08.250

Ni, Z., Dhanak, M., & Su, T. (2019). Improved performance of a slotted blade using a novel slot design. *Journal of Wind Engineering and Industrial Aerodynamics*, *189*, 34–44. https://doi.org/10.1016/j.jweia.2019.03.018

Raffel, M., Willert, C. E., Scarano, F., Kähler, C. J., Wereley, S. T., & Kompenhans, J. (2018). *Particle Image Velocimetry: A Practical Guide* (3rd ed.). Springer International Publishing. https://doi.org/10.1007/978-3-319-68852-7

Sathish Kumar, D., & Jayavel, S. (2020). Microchannel with waviness at selective locations for liquid cooling of microelectromechanical devices. *Journal of Applied Fluid Mechanics*, *14*(3), 935–948. https://doi.org/10.47176/jafm.14.03.31874

Sun, J., Gao, T., Fan, Y., Chen, W., & Xuan, R. (2019). The modulation of particles on coherent structure of turbulent boundary layer in dilute liquid-solid two-phase flow with PIV. *Powder Technology*, *344*, 883–896. https://doi.org/10.1016/j.powtec.2018.12.044

Wan, Z., Wang, Y., Wang, X., & Tang, Y. (2018). Flow boiling characteristics in microchannels with half-corrugated bottom plates. *International Journal of Heat and Mass Transfer*, *116*, 557–568. https://doi.org/10.1016/j.ijheatmasstransfer.2017.09.029

Wang, H., Liu, B., Zhang, B., & Chen, C. (2021). Impact evaluation of full-span slot and blade-end slot on performance of a large camber compressor cascade. *Journal of Applied Fluid Mechanics*, *14*(4), 1113–1124. https://doi.org/10.47176/jafm.14.04.32273

Wang, L., Luo, X., Feng, J., Lu, J., Zhu, G., & Wang, W. (2023). Method of bionic wavy tip on vortex and cavitation suppression of a hydrofoil in tidal energy. *Ocean Engineering*, *278*, 114499. https://doi.org/10.1016/j.oceaneng.2023.114499

West, G. S., & Apelt, C. J. (1982). The effects of tunnel blockage and aspect ratio on the mean flow past a circular cylinder with Reynolds numbers between 10 4 and 10 5. *Journal of Fluid Mechanics*, *114*(1), 361.

https://doi.org/10.1017/S0022112082000202

Yang, H., Lang, B., Du, B., Jin, Z., Li, B., & Ge, M. (2022). Effects of the steepness on the evolution of turbine wakes above continuous hilly terrain. *IET Renewable Power Generation*, *16*(6), 1170–1179. https://doi.org/10.1049/rpg2.12420

Zhang, E., Wang, X., & Liu, Q. (2022). Numerical investigation on the temporal and spatial statistical characteristics of turbulent mass transfer above a two-dimensional wavy wall. *International Journal of Heat and Mass Transfer*, *184*, 122260. https://doi.org/10.1016/j.ijheatmasstransfer.2021.122260

Zilker, D. P., & Hanratty, T. J. (1979). Influence of the amplitude of a solid wavy wall on a turbulent flow. Part 2. Separated flows. *Journal of Fluid Mechanics*, *90*(2), 257–271. https://doi.org/10.1017/S0022112079002196